Development of Micromegas detectors with resistive pads

M. Chefdeville[a,*], C. Drancourt[a], N. Geffroy[a], T. Geralis[b], A. Kalamaris[b], Y. Karyotakis[a], D. Nikas[b], F. Peltier[a], A. Psallidas[b], M. Titov[c], G. Vouters[a]

[a] *Univ. Grenoble Alpes, Univ. Savoie Mont Blanc, CNRS, IN2P3-LAPP, Annecy, France*
[b] *INPP, NCSR Demokritos, Agia Paraskevi, Attiki, Greece*
[c] *IRFU, Saclay CEA, Gif-sur-Yvette, France*

Abstract

A novel type of resistive Micromegas combining a Bulk mesh and a resistive pad board is presented. Readout pads are covered by a thin insulating layer with a top resistive coating segmented into resistive pads. Readout and resistive pads are electrically connected by means of planar resistors embedded in the insulator, enabling fast clearance of the avalanche charge from the resistive surface. With a suitable choice of the resistance, this detector operates linearly and without sparks at X-ray flux several orders of magnitude beyond what non-resistive Micromegas sustain, up to $\sim 1\,\mathrm{MHz}\,/\,\mathrm{mm}^2$. Testing $10 \times 10\,\mathrm{cm}^2$ prototypes of different resistance in a hadron beam, stable operation or sparking were observed, providing an empirical limit on the minimal resistance to avoid sparks. Response to electromagnetic showers in the 30–200 GeV energy range was also measured by means of a small calorimeter combining six resistive prototypes and iron absorbers. Results are well reproduced by a Monte Carlo simulation, pointing at negligible resistivity-induced charge-up effects in the experimental conditions. Finally, the scalability of the manufacturing process to larger detector sizes is demonstrated by successful operation of three $50 \times 50\,\mathrm{cm}^2$ resistive prototypes with embedded front-end electronics. Interestingly, it is found that passive protections of the electronics against sparks (diodes on a printed circuit board) are not required in such resistive detector designs.

*Corresponding author
Email address: chefdevi@lapp.in2p3.fr (M. Chefdeville)

Keywords: Micro Pattern Gas Detectors, Micromegas, resistive electrodes

1. Introduction

Owing to the small anode-to-cathode distance ($\sim 100\,\mu$m) in Micro Pattern Gas Detectors (MPGD), the fast removal of positive ions by nearby electrodes results in a short collection time and eliminates space charge build-up [1, 2]. MPGDs therefore show excellent rate capability [3] and are good candidates for experiments at high luminosity colliders (LC [4, 5, 6, 7], HL-LHC [8], CEPC [9] and FCC [10]). Occasional sparking could be a serious flaw for such applications but can be suppressed by means of resistive electrodes. Spark-free operation can be achieved with different resistive materials (glass, DLC [11, 12]) and detector designs, most often using a resistive layer but also resistive patterns.

In a detector without mechanical imperfections, sparks are triggered by an ionisation event when the total size in the avalanche exceeds a critical charge density; this is known as the Raether limit ($\sim 10^8$ electrons) [13]. It indicates the transition from avalanche to streamer mode which might occur when too many primary electrons are released in the gas (by *e.g.* an α particle), or when an electron avalanche generates successor avalanches through feedback mechanisms [14, 15]. Diverging processes nevertheless, can be impeded by means of resistive electrodes. Progressive charge-up of the anode by avalanche electrons reduces locally the electric field and quenches the spark at an early stage of development. Due to the finite resistivity of the electrode, the surface charge is eventually drained to ground and the local field is restored after a characteristic time.

In a simple detector design, an insulating foil with a resistive surface coating is coupled to the readout plane. Signal induction is controlled by the electric properties of the foil and coating, while surface charges are drained to ground at the edges of the foil where proper connections are made. This grounding scheme is not suited for large detector sizes and operation at high particle rates due to slow evacuation and pile-up of surface charges and the resulting drop of gas gain. To mitigate this, a new design using shorter electrical paths to ground is proposed: the resistive layer is segmented into resistive pads which are connected to ground by means of resistors embedded in the insulator. Embedded resistors were initially proposed by Oliveira *et al.* [16] and first implemented in COMPASS prototypes using a few mm^2 pads and a relatively large resistance [17]. More recently and in parallel to this work, prototypes with large pads of $1 \times 1\,\mathrm{cm}^2$ were studied for the ATLAS experiment [18], where the possibility to use a continuous resistive coating was also explored [8].

In this contribution, small-size prototypes of various pad resistance were extensively tested. Non-resistive prototypes were also constructed to give a point of reference. The fabrication process is described in section 2. Results on gas gain, signal linearity, rate capability and stability to hadrons, which were partly published in [19], are reported in section 3 to 7. Measurements of electron showers in a small calorimeter are reported in section 8 where a detailed simulation model is presented.

Larger area prototypes were subsequently built to verify the scalability of the fabrication process. Their design inherits from previous R&D on Particle Flow calorimetry where the front-end electronics is integrated directly on the Bulk Micromegas pad board [5]. Diodes placed between electronic channel inputs and readout pads absorb the energy of sparks which could otherwise destroy sensitive circuits. Three prototypes were equipped with a resistive Micromegas, including one without diodes to assess the protection capability of the resistive electrodes itself. A fourth prototype was equipped with an RPWELL [7]. Having four detectors, pad-to-pad efficiencies were measured with an in-situ method. Results are reported in section 9.

2. Detector design

2.1. Fabrication process

All prototypes are composed of a board with $1 \times 1\,cm^2$ pads, a Micromegas and a resistive stage. The latter is a sandwich of kapton foils and screen-printed resistive paste and is fabricated as follows. A 25 μm kapton foil is first glued onto the pad board. Small holes are drilled into the foil and filled with silver paste to later provide an electrical contact between metallic pads and embedded resistors. A 50 μm photosensitive film (coverlay) is then laminated onto the board and etched to the chosen resistor shape. Etched spaces are filled with resistive paste by screen-printing. The paste is baked and its surface polished. A second kapton foil is then glued and drilled to create the silver vias that will connect resistors to resistive pads. As for the embedded resistors, a second photosensitive film is used to make resistive pads. The shortest distance between two adjacent resistive pads is 500 μm, resulting in 10 % inactive regions. After polishing and cleaning, the board is finally equipped with a Bulk Micromegas [20]. The final detector design is illustrated in Fig. 1 (top). The distance from the anode pad surface to the resistive pad surface is 150 μm while the amplification gap between the resistive pad and the mesh is 120 μm.

2.2. Small prototypes

Small prototypes are built on $20 \times 30\,\mathrm{cm}^2$ printed circuit boards (PCB). The active region is a 10×10 matrix of $1 \times 1\,\mathrm{cm}^2$ copper pads. One of the four corner pads is used to bias the mesh while the other are filled with coverlay. The 96 other pads are routed to a connector for Gassiplex electronic boards (when anode signals are read out) or for direct grounding (when mesh signals are read out). In the latter case, signals are digitised by a multi channel analyser (Amptek's MCA-8000D).

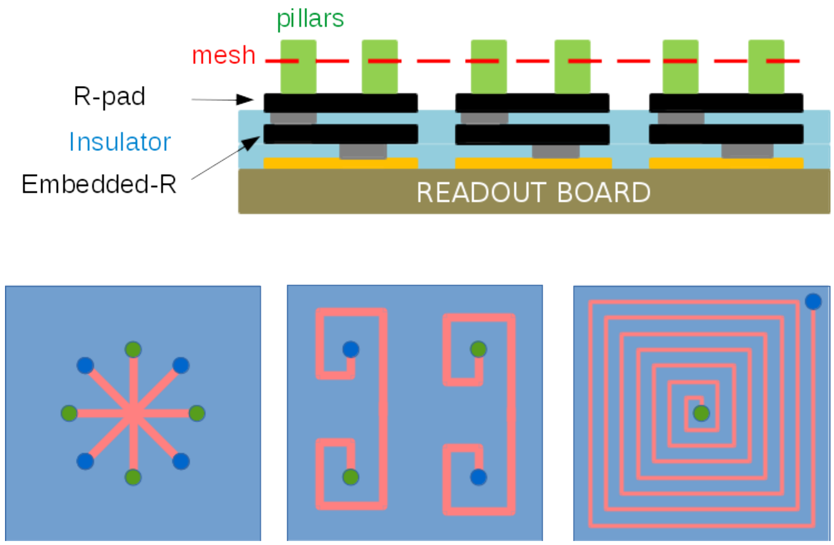

Figure 1: Not-to-scale drawing of a Micromegas with embedded resistors (top). Resistor shapes (bottom), from left to right: star, mirror and snake shapes. Blue (green) dots are electrical connections between the embedded resistor and the resistive (metallic) pads.

A first batch of three prototypes was produced using a paste with a sheet resistance R_S of $100\,\mathrm{k}\Omega/\square$. After successful tests, a second batch with $R_S = 1\,\mathrm{k}\Omega/\square$ was produced. For a given resistivity, the pad-to-ground resistance is given by the shape of the embedded resistor and the number of vias (Fig. 1 (bottom)). Vias act as a current divider and could influence the detector behaviour at high rates. The following designs were studied:

- *star*: 4 parallel resistors in series with 4 parallel resistors, and 8 vias;
- *mirror*: 2 parallel resistors and 4 vias;
- *snake*: one resistor and 2 vias;
- *spider*: is a *snake* pattern with strip-patterned resistive pads.

During fabrication, the resistance between top vias and ground was measured with an ohmmeter for several pads of the first batch prototypes. A uniformity of 10 % RMS is achieved. Average values are ~ 1, 4 and $40\,\mathrm{M}\Omega$ for star, mirror and snake pattern respectively. Values for the second batch should be 100 times smaller.

Some measurements were performed in a dedicated gas vessel where each prototype was successively placed (section 4.1). Later on, they were individually equipped with a drift cover in steel, defining a 3 mm drift gap. Small openings in the cover serve as X-ray windows. Unless stated otherwise, a mixture of Ar/CO_2 93/7 is flushed through the chambers.

2.3. Large prototypes

Large resistive prototypes are built on $50 \times 50\,\mathrm{cm}^2$ PCB with anode pads on one side and front-end Application Specific Integrated Circuits (ASIC) on the other side. These so-called Active Sensor Units (ASU) previously developed for hadronic calorimetry are described in details in [5]. The initially rectangular pad array was changed to a circular array to provide uniform radial containment of particle showers. An intermediate board collecting the ASIC data and providing high-voltage to the detector was also merged to the ASU. Based on the experience with small prototypes, a resistance of $\sim 1\,\mathrm{M\Omega}$ ($R_\mathrm{S} = 100\,\mathrm{k\Omega}/\square$) using a snake pattern was chosen for the three large prototypes.

3. Gas gain and energy resolution

3.1. Introduction and calibration

The gas gain of the small prototypes is measured using X-rays from a Cu target X-ray tube (K_α line at 8.1 keV). First, the X-ray tube is used to derive an absolute reference gain G_ref by measuring the mesh current i_mesh in the non-resistive prototype and the photon conversion rate f:

$$G_\mathrm{ref} = \frac{i_\mathrm{mesh}}{f N_\mathrm{p} q_\mathrm{e}} \qquad (1)$$

where N_p is the average number of primary electrons released in the gas and q_e is the electron charge. Next, the relative gain dependence on mesh voltage is measured by recording the total charge spectrum with the MCA and extracting the magnitude of the photoelectric peak from a fit. Relative gains are then converted to absolute gains using G_{ref}.

As pile-up conditions at mid-range tube power prevent a direct measurement of the conversion rate, a thin absorber consisting of a copper tape is placed on the detector window to reduce the rate down a few hundreds of kHz which can be accurately measured with the MCA. The resulting current attenuation determined as the current ratio without and with foil is then used to calculate the rate without the foil: $f \sim 56\,\mathrm{MHz}$.

A typical MCA spectrum of X-ray conversions is shown in Fig. 2 where the photopeak, the escape peak and a bremstrahlung continuum are visible. After fitting these contributions to the data points, the ratio R between the average ADC value and the most probable ADC value of 0.89 is used to calculate the average number of primary electrons entering Eq. 1: $N_p = RE_\alpha/W \sim 268$, where $E_\alpha \sim 8.1\,\mathrm{keV}$ is the energy of the K_α line of copper and $W \sim 26.9\,\mathrm{eV}$ the mean energy per ion pair in the gas mixture. The average ADC value is calculated from the fit function to account for events below the MCA threshold.

3.2. Gain curves

Gain measurements are performed at a rate of a few kHz. X-rays are collimated to the centre of a pad such that inactive dielectric regions between resistive pads have negligible impact on the measurement. At each mesh voltage, the ADC counts spectrum is recorded and the gain calculated using the previous calibration. Results are summarised in Fig. 3.

All prototypes operate at a maximum gain of $1\text{–}2 \cdot 10^4$. The mesh voltage applied to reach a given gain varies by $\sim 30\,V$ between the two batches of resis-

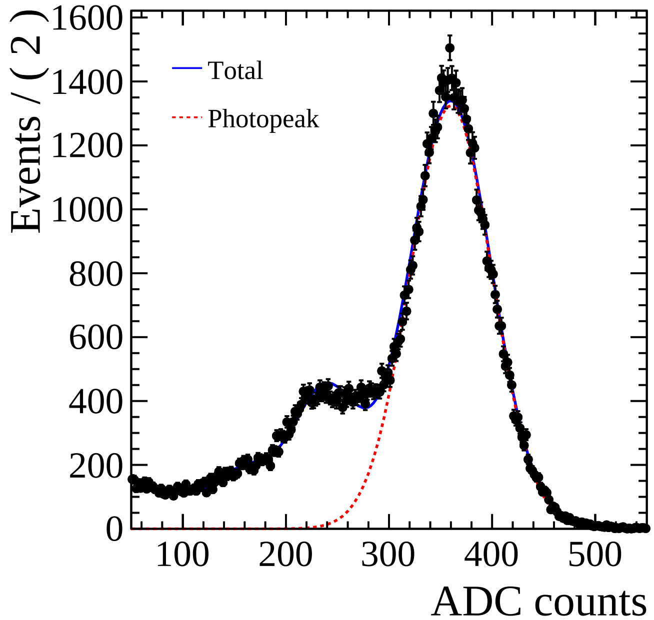

Figure 2: Energy spectrum of X-ray tube photon conversions measured with a non-resistive prototype. The red-dashed line represents the contribution of the 8.1 keV K_α line of copper.

tive prototypes, while the response of the non-resistive prototype, constructed first, lies in between. This small dispersion reflects the thickness uniformity of the coverlay foils used to make the mesh pillars. Thickness variations from different rolls of 64 μm coverlay foils are guaranteed at the $\pm 7\,\mu m$ level. As two foils are laminated on the pad boards, prototypes from different batches can show very different gains. As an example, Monte Carlo simulations of the avalanche process in the gas mixture used, predict a relative gain increase of $\sim$1.7 for a -14 μm variation from a nominal 128 μm thickness [21].

Prototypes from the 100 k$\Omega/\Box$ batch have comparable gas gains. The spectra in Fig. 4 also reveal a worse energy resolution (a factor 2) of the mirror, star and spider-like prototypes with respect to the snake-like prototype which achieves 30% FHWM, compared to 23% for the non-resistive prototype. A noticeable feature in the 100 k$\Omega/\Box$ prototype distributions is the tail on the right-hand

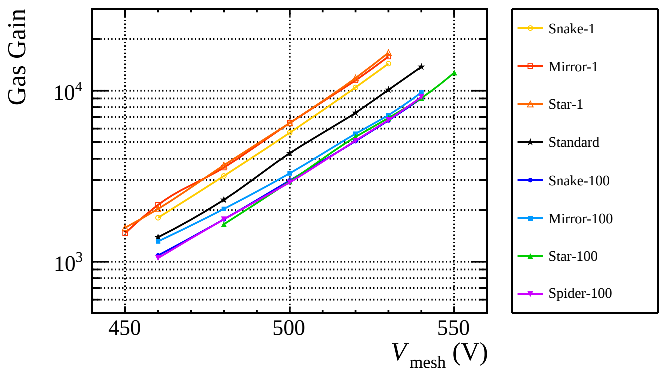

Figure 3: Gas gain versus mesh voltage measured in Ar/CO_2 93/7 using a Cu target X-ray tube. Measurements with a standard non-resistive prototype are plotted with black star-shaped markers. Other data points correspond to resistive prototypes. The legend indicates the pattern of the embedded resistor (as explained in the article) and its surface resistance (1 k$\Omega/\square$ or 100 k$\Omega/\square$).

side of the photopeak which points to regions of higher gains and therefore poor response uniformity. The flatness of the resistive pad surface is indeed crucial to define a constant amplification gap but seems to be mediocre for this firstly produced batch. Lower resistivity prototypes (1 k$\Omega/\square$) show an improved energy resolution of about 30% FWHM for the three designs, with again best results for the snake-like design.

4. Signal linearity with a charge injector

Accumulation of electric charge at the surface of the resistive layer can result in significant reduction of gas gain. The surface charge distribution reflects the arrival of avalanche electrons at the resistive surface which depends on the gas gain, event rate and type of ionising radiation (*e.g.* minimum ionising particles, X-rays, α particles). It is therefore interesting to study the rate dependence of the response (in section 5) and if proportionality is preserved at high resistivity [22] or high primary charge. Following a setup described in [23], resistive prototypes are successively tested in combination with a GEM foil that acts as a

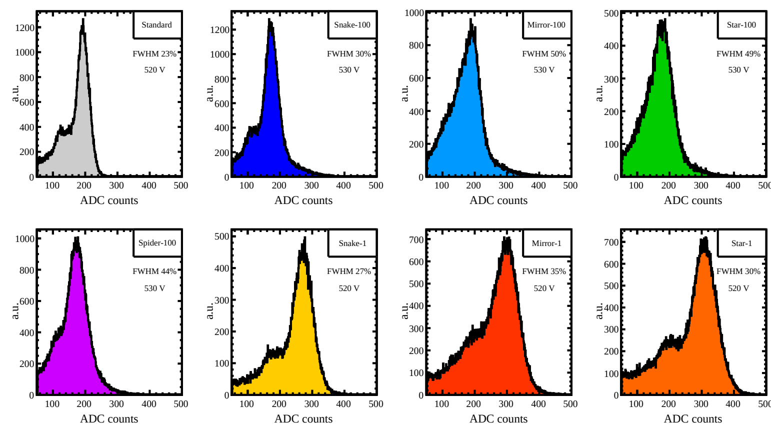

Figure 4: Multi-channel analyser output distributions measured in Ar/CO_2 93/7 using a Cu target X-ray tube (mesh voltage between 520–530 V).

first amplification stage.

4.1. Experimental setup

A dedicated gas vessel with a kapton-based drift electrode is flushed with Ar/CO_2 90/10. It contains a $10 \times 10\,\mathrm{cm}^2$ standard GEM foil (140 μm hole picth, 70 μm hole diameter) placed 3 mm above the Bulk mesh to define a 15 mm thick drift region. The extraction field is set to 1.3 kV/cm as a balance between mesh transparency and GEM extraction efficiency, while a drift voltage of 500 V guarantees a good field uniformity and transmission of electrons through the GEM holes. Conversions from 5.9 keV X-rays from an 10 kBq ^{55}Fe source are recorded during two test campaigns (one for each resistivity batch) using the same readout as for previous gain measurements.

4.2. Calibration of the GEM injector

The effective gain is deduced from ^{55}Fe photon mesh signals at different voltages across the GEM electrodes. At $\Delta V = 0\,\mathrm{V}$ across the electrodes, only photons converting between the mesh and the GEM are observed: photoelectric signals are digitised around position p_1. Increasing ΔV, conversions above the

GEM are recorded as well and signals are digitised around position p_2. Fig. 5 shows a spectrum where the two photon populations are well separated.

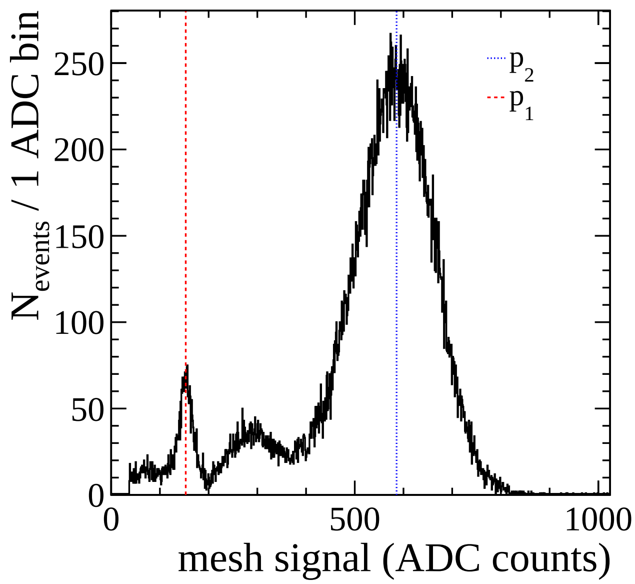

Figure 5: Pulse height histogram when coupling a non-resistive Bulk Micromegas to a GEM pre-amplification stage. The fine-dashed red line at p_1 corresponds to ^{55}Fe photons converting between the GEM and the Bulk. The dashed blue line at p_2 is for conversion above the GEM.

The ratio p_2/p_1 should be a direct measure of the effective gain. As shown in Fig. 6, effective gains up to several hundreds are achieved. Given the relatively small dynamic range of the preamplifier, the GEM gain had to be measured at three different Micromegas gains ($\sim$ 10^2, 10^3 and 10^4 at 390, 460 and 530 V respectively). At decreasing mesh voltage, the Micromegas electron collection efficiency is slightly lower. The measurements at 460 and 390 V are thus scaled up using the well-known collection curve of the Micromegas (by 8% and 22% respectively). Furthermore, the peak position p_1 was only measured at 530 V. At lower Micromegas gains, photon conversions above and below the GEM can't be separated anymore, so p_1 is extrapolated at 460 and 390 V using the known slope of the gain curve. The three gain curves of the GEM overlap well, as shown in Fig. 6. A slight change of slope is observed which can be explained by a more favorable field configuration close to the GEM holes at larger ΔV.

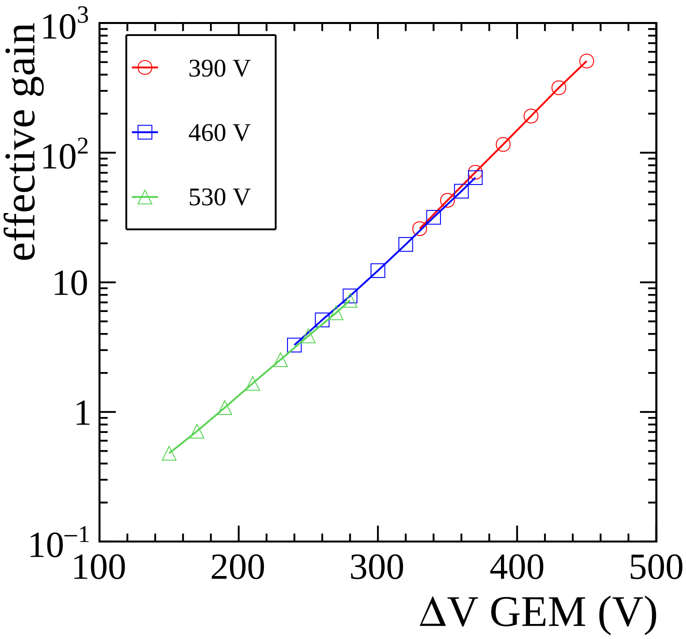

Figure 6: Effective gain of the GEM foil measured at different Micromegas mesh voltages.

4.3. Response of resistive prototypes

The response of resistive prototypes is defined as the ^{55}Fe photopeak position p_2 as a function of the GEM effective gain from Fig. 6. Prototypes of $100\,\mathrm{k}\Omega/\Box$ were operated at gains of $G \sim 10^2$, 10^3 and 10^4. Although the charge range is similar during the three scans, the charge density on the pad surface should be higher in the last case and could reveal a different behaviour. This is however not observed and all measured responses are fairly linear over the tested range. This is illustrated in Fig. 7 where the best straight line fit is added to each measured response. As opposed to [19] where the straight line was forced to the origin, the intercept with the vertical axis is now floated to allow for a non-zero pedestal at the MCA input (this pedestal could not be measured).

If the pedestal is not zero, the data points (mainly those with low p_2 values) are shifted from their true values, yielding a non-physical response. In Fig. 7, points at low p_2 indeed stand below the fit which could, as occurred in [19], be misinterpreted as saturation.

During the second test period, the preamplifier dynamic range was extended by reducing its gain by a factor 3.5. A single scan was performed for each 1 kΩ/□ prototype at a gas gain close to 10^4 ($V_{\mathrm{mesh}} = 510\,\mathrm{V}$). Response curves are shown in Fig. 8 and are linear as well, which is compatible with the performance at higher resistivity.

5. Rate capability with X-rays

Rate capability is a flagship measurement for resistive detectors. It indicates if sparking is suppressed and if the magnitude of charge-up effects is governed by the Ohm's law. Measurements reported in this section were performed first with the 100 kΩ/□ prototypes. When the second batch became available, the measurements were repeated, although at lower rates due to using a different apparatus. Results from the two test campaigns are consistent.

5.1. Experimental setup and protocol

The setup is the one used for the gain measurements (section 3). Photons from the X-ray tube are collimated to a 3 mm diameter spot at the detector window. One pad is illuminated so the current flows through one embedded resistor only. Results are easier to interpret this way and charge-up effects are maximal. The X-ray tube power is converted into a particle flux using the rate calibration of section 3.1 and the known beam spot size. During the first test campaign, four rate scans were performed per prototype (at 400, 435, 470, 505 V). Due to a larger number of prototypes and time constrains in the laboratory, this was reduced to a single scan during the second campaign.

5.2. First test campaign

Response curves obtained with the $100\,\mathrm{k}\Omega/\square$ prototypes are shown in Fig. 9 where the non-resistive best measurement was added for reference (best meaning that sparking was sufficiently rare to measure stable currents). Below 470 V, the responses are linear and therefore not shown. At 470 V and 505 V, the response of all resistive prototypes saturates. In the absence of saturation, the expected gains would be $\sim 1.5\cdot 10^3$ and $\sim 3.5\cdot 10^3$ respectively.

At given rate and voltage, prototypes with higher resistance exhibit more saturation. For a given prototype, saturation is also more pronounced at high rates due to an increased voltage drop across the amplification gap. Ignoring space charge effects and charge recombination in the drift region, the current i and rate f are related by:

$$i(f) = i_0(f)e^{-B\Delta V} = Q_0 f e^{-BRi} \tag{2}$$

where i_0 ($Q_0 = q_\mathrm{e} N_\mathrm{p} G$) is the current (average charge per event) in absence of charge-up and is modulated by the gain drop expected from the Ohm's law (B is the slope of the gain curve and R the pad to ground resistance). For small voltage drops ΔV, the exponential can be replaced by its first-order Taylor expansion:

$$i(f) = \frac{Q_0 f}{1 + BRQ_0 f} \tag{3}$$

which is valid to a few percent accuracy for $\Delta V \leq 10\,V$ (*i.e.* a gain drop below 25 %). This assumption should be valid for the star-like and mirror-like prototypes for which the parameters Q_0 and BR can be accurately fitted to the data. The resulting fits are superimposed on the data points. The expected response in absence of charge-up is also indicated. Deviations from the linear response are essentially governed by the voltage drop which can be calculated from the fit parameters. Results are summarised in Fig. 11 where the voltage drop is plotted against mesh current. Ohm's law is well verified except for the highest-R prototype (snake pattern) which expected non-saturated response can not be precisely derived because Eq. 3 is a poor approximation. In that case, the non-saturated response is taken from a fit to the lowest voltage scan data (400 V) and extrapolated to higher voltages using the measured slope of the gain curve. The limited precision of this extrapolation might explain the departure from Ohm's law seen in Fig. 11.

5.3. Second test campaign

The X-ray tube power during the second campaign was smaller by a factor ten. After rate calibration, scans were repeated or performed for the first time. Repeated measurements are well compatible with those of the first campaign and labelled in Fig. 9 as tube 2. Performance of $1\,\mathrm{k}\Omega/\Box$ prototypes measured at $\sim 490\,\mathrm{V}$ (*i.e.* gas gain of $\sim\ 5\cdot 10^3$) are shown in Fig. 10. Only snake and spider-like prototypes exhibit a slight saturation due to a higher resistance. Despite the low resistivity used, it is remarkable that stable operation is achieved at such high rates and gas gain.

6. Discharge rate measurements with X-rays

Although sparks were not seen when operating the prototypes in current mode, a complementary study was performed in pulse mode using a differentiator circuit with a large time constant ($RC = 0.1\,\mathrm{s}$) to read out the mesh electrode. The mesh was connected to a 10 nF capacitor and then a 10 MOhm resistor to the ground. The signal was probed from the resistor to a shaper - amplifier with unit amplification. As verified with Spice simulations ([24]), signal frequencies above 30 Hz are fully transmitted, thus the voltage drop of ionising events can be recorded by measuring the pulse height. Spectra of voltage drops were recorded for long periods of irradiation with X-rays (Rh 3 keV X-ray tube) at a high rate with the spider-like prototype ($R = 1.5\,\mathrm{M}\Omega$). The Rh X-ray tube operated at 5 kV produces 3 lines of close energy (2.69 keV - 67%, 2.83 keV - 26.8 %, 3.0 keV - 6 % and a negligible continuum) averaging at 2.75 keV. Garfield++ simulation shows that from each 2.75 keV X-ray, 101 ± 13 primary electrons are produced. In order to increase the photon conversion rate a drift gap of 1.4 cm was used in this setup. The irradiated area was about $0.18 cm^2$ and the observed currents were up to 90 nA depending on the gain. The detector linearity was excellent for rates up to 10s of MHz/cm^2.

Table 1 shows the voltage drop rates for gain spanning from 2–6×10^3 at a constant rate of 11 MHz/cm^2 for periods of 24 hours. The third column refers to rates with voltage drop larger than 30 mV, which corresponds to a charge pulse just above the Raether limit ($10^8\,e$), taking into account the detector capacitance ($\sim 600\,pF$). The fourth column refers to discharge rates with voltage drop larger than 0.5 V, corresponding to small but measurable gain drop. The maximum voltage drop never exceeded 0.8 V for gains up to 4000 while for a gain of 6000 it was at most 2 V with an extreme case of 4.9 V. At a gain of 2000, no voltage drop greater than 0.5 V was recorded over a period of 24 hours, corresponding to a relative gain drop below 2 % (as deduced from the slope of the gain curve in Fig. 3). At such rates and gas gains, sparking has thus a negligible impact on the detector performance.

7. Stability with pion showers

Successful operation of resistive prototypes at gains and X-rays fluxes unsustainable by a standard Micromegas suggests a suppression of sparking already at very low resistance values. The charge deposited by X-rays in the gas, however,

Table 1: Rates of events provoking a voltage drop larger than 30 mV (r_1) and 0.5 V (r_2) under 11 MHz/cm^2 X-rays illumination.

Gain	Maximum HV drop (V)	r_1 (/cm^2/s)	r_2 (/cm^2/s)
2000	0.25	5.5×10^{-4}	1.3×10^{-4}
3000	0.80	1.4×10^{-3}	2.8×10^{-4}
4000	0.80	2.7×10^{-3}	6.8×10^{-4}
6000	4.90	1.8×10^{-1}	1.4×10^{-1}

is at most a few hundreds primary electrons. In these conditions, sparks mainly occur by superposition in time and space of close-by photon conversions. On the other hand, hadrons might release heavily ionising particles with energies in the MeV range. Tests with hadrons are therefore necessary to evaluate spark suppression in a definitive manner. This is done by measuring the mesh current in an intense hadron beam at CERN.

7.1. Experimental setup

High-energy 150 GeV/c pions produced in the interaction of the SPS proton beam with targets are directed to the North Area of CERN in the H4 beam line. The detector stack is composed of nine small Micromegas (seven of which are resistive) held perpendicular to the beam direction and biased at 470 V. The pion beam has a $\sim 1 \times 1\,\mathrm{cm}^2$ transverse size and its rate is about 200 kHz. To enhance the number of particles traversing the detector, a $1.5\,\lambda_{\mathrm{int}}$ thick iron brick is placed ~ 1 cm upstream of the prototype under test. Mesh and drift currents are recorded and analysed offline.

7.2. Results

Typical current recordings from non-resistive and resistive prototypes are shown in Fig. 12. In the first case, the mesh current is quite irregular with spikes to several μA interpreted as frequent sparking. On the other hand, most resistive prototypes show reduced and stable currents which can be explained as an absence of sparking.

Currents at the highest pion rate are binned into histograms to make an easier comparison. Histograms are plotted in Fig. 13. Except for the lowest resistance prototype, mesh currents are roughly constant: current distributions show a peak at $\sim 200\,\mathrm{nA}$ and $\sim 500\,\mathrm{nA}$ for the 100 and $1\,\mathrm{k}\Omega/\square$ prototypes respectively. The current ratio between the two resistivity values is consistent with the known gain curves. Interestingly, the behaviours of the lowest resistance prototype and standard Micromegas are similar, which suggests that sparks are suppressed if the resistance is larger than a threshold value.

The physical meaning of this threshold resistance is unknown. As an outlook to future investigations, we propose that it reflects a competition between the physical processes that charge-up the resistive elements (avalanche growth) and those that discharge it (RC constant). If the electric field is restored too quickly, electron avalanches can diverge and lead to a spark. If not, charges pile-up and quench the spark by Ohmic voltage drop. In this model, sparks are suppressed if the RC constant is larger than the timescale of the avalanche development ($\sim 1\,\mathrm{ns}$). Examination of the validity of this model involve measurement and modelling of the time response of the resistive detectors and should be part of future work.

8. Response to electromagnetic showers

Modelling and measuring the detector response and scrutinizing the level of agreement between them offers a ground for testing the understanding of the underlying physical processes. This approach is followed using electrons in the 30–200 GeV range showering in a small calorimeter of six prototypes (two standard and four resistive) and iron absorbers. The total charge per shower is measured at different energies and compared to simulation. All prototypes are simulated nearly in the same way (*i.e.* the resistive layer is ignored) except for variations in average gas gain. As will be shown, this approximation is good enough to reproduce the data.

8.1. Experimental setup

Four $100\,\mathrm{k}\Omega/\square$ resistive prototypes and two non-resistive prototypes from the SPS/H4 setup described in section 7 were used. Adding iron absorbers between the prototypes (Fig. 14), a calorimeter thickness equivalent to $\sim 23\,\mathrm{X}_0$ and $\sim 2.4\,\lambda_{\mathrm{int}}$ is achieved which is sufficient to contain the electron showers.

Individual pads are read out by Gassiplex electronics upon reception of a scintillator trigger and digitised with 10-bits resolution (see [25] for details). A working voltage of 470 V was chosen as a compromise between high signal-over-noise ratio and rare ADC saturation. The beam was set at six energy points (30, 50, 70, 90, 130 and 200 GeV) with almost constant transverse size and rate ($\sim 1 \times 1\,\mathrm{cm}^2$ and 1–2 kHz). Its composition is energy-dependent with *e.g.* a pion fraction of 30 % at 200 GeV. This contamination is reduced offline using the first calorimeter layer as a preshower. About 5×10^4 events were recorded at each energy.

8.2. Simulation

The Monte Carlo (MC) Geant4 software toolkit (version 10.5, [26]) is used to model the calorimeter and simulate the development of showers (the beam line instrumentation is ignored). Geant4 energy deposits in the gas are digitised by a standalone program which shifts and smears the beam position. Primary electrons are generated according to the W value of the gas mixture. The avalanche process is using the individual gas gains of section 3, assuming exponential fluctuations. Next, the number of electrons to ADC counts conversion is performed using the electronic gain from the Gassiplex data-sheet. Measured pedestals are subtracted from the ADC counts. If the difference is above 2^{10}, the ADC value is set to 1024 to account for saturation. Finally, the event reconstruction proceeds the same for simulated and real data. For each detector channel, the ADC value is compared to a threshold equal to ten times the pedestal noise. A signal above threshold is counted as a hit.

Electrons and pions samples are generated at each energy point. Pion samples serve the definition of various cuts applied to real data to improve the electron purity. For this purpose, 10^4 pion events per energy point are sufficient. To align with the statistics in real data, 4×10^4 electron events are simulated at each energy.

8.3. Event selection and charge fits

Electromagnetic and hadronic showers leave different signature in the calorimeter. Pions traversing the calorimeter without showering leave roughly one hit per active layer and are easily identified. Late-showering pions can be suppressed using the energy-weighted barycentre along the beam direction which is relatively small for electrons. Larger fluctuations in the transverse development of pion showers provide additional handles. To reduce lateral energy leakage, fiducial cuts on the horizontal and vertical barycentres are also applied. Cut values are deduced from simulation. Selection efficiencies are about 95 % for electrons and 14 % for pions (Table 2).

8.4. Results

Total charge distributions after selections are shown in Fig. 16 where the MC distributions are scaled to the data statistics. A good overall agreement is found. Calorimeter performances are fitted to the data points. Since electron samples are very pure, their charge distribution is modelled by a Novosibirsk

E_{beam} (GeV)	30	50	70	90	140	200
ϵ_{e^-} (%)	95.1	94.6	93.4	93.4	96.0	96.0
ϵ_{π^-} (%)	15.8	14.8	13.0	12.9	14.5	15.5
$N_{\text{e}} \times 10^{-3}$	37	35	30	25	33	26
$(\mu_{data} - \mu_{MC})/\mu_{MC}$ (%)	-2.0	5.2	-0.7	1.1	-0.2	-3.4
$R_{data} - R_{MC}$ (%)	1.3	0.5	1.1	0.7	0.6	0.6

Table 2: Expected selection efficiency for electrons and pions versus energy. The middle rows indicate the number of selected electron events in the data. Data/MC agreement for the average charge (μ) and resolution (R) is indicated in the last two rows.

function (defined in Appendix A) to accounts for an eventual radiative tail. The electron response shown in Fig. 15 (top) is the relation between the mean total charge μ and the electron energy. Charge resolution calculated as $\sigma\,/\,\mu$ improves with energy (Fig. 15 (bottom)) as expected from the stochastic fluctuations of the shower process. Simulation results are included in the figures. The MC response agrees with data at the $\sim$ 5% level (Table 2) while simulated charge distributions are always slightly narrower. A small offset of 1 % in data might be due to pad-to-pad gas gain variations which are not modelled. The overall scale and trend are nevertheless well reproduced and no striking features from using resistive Micromegas are observed.

9. Large resistive prototypes

Following a detailed exploration of the parameter space of small prototypes, three prototypes of larger size ($\sim\ 0.2\,m^2$) using snake-like embedded resistors (R =, $1\,M\Omega$ with $R_{\text{S}} = 100\,\text{k}\Omega/\square$) were constructed and tested to demonstrate that the manufacturing process can be used for larger PCBs. Two of them are equipped with diodes to protect the front-end electronics against discharges. The third prototype features only the resistive electrodes to ultimately test the suppression of sparks for this type of resistive Micromegas.

9.1. Resistive Active Sensor Units and test setup

Compact detector designs for sampling calorimetry at a future e^+e^- linear collider are studied by the CALICE collaboration. In these designs, the front-end electronics and the sensitive medium are held on a same support (a PCB) to allow for very-high granularity. A Micromegas design was proposed and studied using $1 \times 1\,\mathrm{m}^2$ prototypes, each composed of so-called Active Sensor Units (or ASU) placed inside a common gas vessel [5]. The ASU consisted of a Bulk Micromegas laminated on a 1.2 mm thin PCB with pads on one side and diode-protected front-end chips (or ASICs) on the other side. This detector was not resistive and subject to sparking [27]. A natural evolution was to make it resistive. The resistive ASUs are equipped with 1792 readout pads forming a circular active area which reflects the rotational symmetry of hadron showers.

9.2. MIP efficiency and spatial uniformity

Given the $\sim$ 20-fold increase of the active area, emphasis was first put on characterising the uniformity of the response by means of a wide 150 GeV muon beam (SPS/H4 beam line). Composed of three resistive Micromegas ASU and a fourth ASU equipped with a large RPWELL electrode [7], the detector stack can be used to measure hit efficiency without external information thanks to a common data acquisition system. The efficiency plateau is first measured locally for one prototype to define a working voltage. The detector stack is then moved horizontally and vertically across the beam at constant voltage to control the uniformity of the response over most of the pads.

Muon trajectories are reconstructed using the time and position of hits in three so-called telescope prototypes: single hits with same pad coordinates and timestamp are required. The efficiency of the fourth test prototype is inferred from the presence of a hit in a small time and space interval around the expected coordinates ($\pm$ 200 ns and $\pm$ 1 pad). Fig. 18 shows the trend of efficiency together with a previous measurement performed with a $1 \times 1\,\mathrm{m}^2$ non-resistive prototype using a different argon-based mixture [5]. The plateau is reached at a different voltage as expected, but the resistive ASU achieves a slightly inferior efficiency by 2–3 %. Inactive dielectric regions between resistive pads could explain this drop. Although mitigated by the transverse diffusion of the electrons in the drift region and not relevant for calorimetry resolution, this effect could be reduced in a future design with wider resistive pads.

Fig. 19 shows two-dimensional efficiency maps obtained at 500 V where the statistical error per pad is below 1.5%. Most probable value and dispersion calculated from a binned fit to the 1D-distributions are listed in Table 3. The measured dispersion is comparable to the statistical error, meaning that it is not significant. To assess the systematic error arising from the size of the search region, the analysis was repeated with larger window sizes, up to ± 7 pads. In that last case, the most probable efficiency increased by $\sim 0.2\,\%$ suggesting that the measurement is robust against noise. If we ignore the data points corresponding to the wrongly configured ASIC, the uniformity is thus given by the statistical error, *i.e.* better than 2%.

Prototype	#1	#2	#3
ϵ_μ (%)	95.6	92.7	97.4
RMS(ϵ_μ) (%)	1.5	1.1	1.0
Δ_ϵ (%)	0.1	0.3	0.1

Table 3: Most probable muon efficiency ϵ_μ measured over the prototype active region using a ± 1 pad search region and its standard deviation RMS(ϵ_μ). The last row reports the efficiency shift Δ_ϵ when using a ± 7 pads search region.

9.3. Stability in a high-intensity pion beam

Detector stability was then studied using a pion beam collimated to a narrow region at the detectors. From the measured beam profile, an intensity of $\sim 0.5\,\mathrm{MHz/cm^2}$ is estimated at the central pad. The mesh voltages of the Micromegas prototypes are raised from 430 V to 540 V in eight increments and the data acquisition system is kept running during the scan. At each voltage increment, the integrity of the front-end electronics is checked by configuring the ASICs and scrutinising the reconstructed beam profile.

Variations of mesh currents are recorded by the RD51 slow-control system (Fig. 20). At a given voltage, all mesh currents are roughly constant during the spills. At equal voltages, larger currents are measured in downstream prototypes due to an increased particle multiplicity along the beam direction when pion shower inside the detector material. All prototypes operate up to the highest tested voltage value which should correspond to a gain of 10^4 as charge-up effects are small ($\Delta V \sim 1\,V$). Most importantly, their behavior are similar and no damage to the readout electronics was observed. The resistive layer solely protects the electronics against sparking and could therefore replace the PCB diode networks in this function. The possible simplification of the PCB design is an important finding in view of a large-scale application at a future physics experiment as both high performance and cost effectiveness are desirable.

10. Conclusions

Embedded resistors are an interesting evolution of resistive layers to improve the rate capability of gas detectors by using a shorter electrical path to ground. Combined with a Bulk Micromegas, they suppress sparking already at surprisingly low values of resistivity (1 k$\Omega/\square$) for which charge-up effects have negligible impact on the detector response, even at very high rates or for large energy deposits. Cross-talk from charge diffusion over the resistive surface can be avoided by segmentation of the layer into resistive pads, at the cost of a few percent loss of MIP efficiency in the studied designs. An important limitation of resistive MPGD is hence lifted as the electric path from pad to ground does not scale with the detector size anymore, which in principle paves the way to the construction of arbitrary large resistive detectors. As a first step in this direction, resistive prototypes of moderate size ($\sim 0.2\,\mathrm{m}^2$) were successfully constructed and operated with high MIP efficiency (95%), excellent uniformity (below 2 %) and no sparks. Replacement of conventional ASIC protection diodes by embedded resistors is an important finding which should simplify the construction of larger detectors and lower their cost.

Appendix A. Fit functions

The Novosibirsk function is given by

$$f(x;\mu,\sigma,t) = \exp\frac{-ln^2(1+t\Lambda\frac{x-\mu}{\sigma})}{2t^2} - \frac{t^2}{2} \tag{A.1}$$

where $\Lambda = \sinh t\sqrt{ln4}/(t\sqrt{ln4})$. This function approaches a Gaussian function when the parameter t vanishes.

Acknowledgements

This work has been partially supported by the RD51 common project SCREAM. Several studies reported in this paper were made using the collaboration infrastructures and hardware. The authors are grateful to the RD51 collaboration for its decisive support. This research was supported in part by the Grant No 5029538 from the Structural Funds, European Regional Development Funds (ERDF) and European Structural Funds (ESF), Greece.

References

References

[1] Y. Giomataris et al. MICROMEGAS: A High granularity position sensitive gaseous detector for high particle flux environments. *Nucl. Instrum. Meth.*, A376:29–35, 1996.

[2] F. Sauli. GEM: A new concept for electron amplification in gas detectors. *Nucl. Instrum. Meth.*, A386:531–534, 1997.

[3] M. Titov and L. Ropelewski. Micro-pattern gaseous detector technologies and RD51 Collaboration. *Mod.Phys.Lett.*, A28:1340022, 2013.

[4] D.C. Arogancia et al. Study in a beam test of the resolution of a Micromegas TPC with standard readout pads. *Nucl. Instrum. Meth.*, A602:403–414, 2009.

[5] C. Adloff et al. Construction and test of a 1x1m^2 Micromegas chamber for sampling hadron calorimetry at future lepton colliders. *Nucl. Instrum. Meth. A*, 729:90–101, 2013.

[6] A. White. Development of GEM-based Digital Hadron Calorimetry using the SLAC KPiX chip. *JINST*, 5:P01005, 2010.

[7] S. Bressler et al. Novel Resistive-Plate WELL sampling element for (S)DHCAL. *Nucl. Instrum. Meth.*, A951:162861, 2020.

[8] T. Alexopoulos et al. A spark-resistant bulk-micromegas chamber for high-rate applications. *Nucl. Instrum. Meth.*, A640:110–118, 2011.

[9] The CEPC Study Group. CEPC Conceptual Design Report, Volume 2. *ArXiv e-prints*, 1811.10545, 2019.

[10] A. Abada et al. FCC-ee: The Lepton Collider Future Circular Collider Conceptual Design Report, Volume 2. *The European Physical Journal Special Topics*, 228:261–623, 2019.

[11] G. Bencivenni et al. The μ-RWELL layouts for high particle rate. *JINST*, 14(5):P05014, 2019.

[12] F. Yamane et al. Development of the Micro Pixel Chamber with DLC cathodes. *Nucl. Instrum. Meth.*, A951:162938, 2020.

[13] H. Raether. *Electron avalanches and breakdown in gases*. Butterworths advanced physics series. London, Butterworths, 1964.

[14] V. Peskov et al. Feedback and breakdowns in microstrip gas counters. *Nucl. Instrum. Meth.*, A397:243–260, 1997.

[15] Yu. Ivanyushenkov et al. Breakdown limit studies in high-rate gaseous detectors. *Nucl. Instrum. Meth.*, A422:300–304, 1999.

[16] R. Oliveira. Resistive ptotections for Bulk Micromegas, Talk given at the 5th RD51 Collaboration Meeting, Freiburg, Germany, May 24-27,2010.

[17] D. Neyret et al. New pixelized Micromegas detector with low discharge rate for the COMPASS experiment. *JINST*, 7:C03006, 2012.

[18] M. Alviggi et al. Construction and test of a small-pad resistive Micromegas prototype. *JINST*, 13(11):P11019, 2018.

[19] M. Chefdeville, Y. Karyotakis, T. Geralis, and M. Titov. Resistive Micromegas for sampling calorimetry, a study of charge-up effects. *Nucl. Instrum. Meth. A*, 824:510–511, 2016.

[20] Y. Giomataris et al. Micromegas in a bulk. *Nucl. Instrum. Meth.*, A560:405–408, 2006.

[21] Georgios Iakovidis. *Research and Development in Micromegas Detector for the ATLAS Upgrade*. PhD thesis, Natl. Tech. U., Athens, 10 2014.

[22] A. Rubin et al. First studies with the Resistive-Plate WELL gaseous multiplier. *JINST*, 8:P11004, 2013.

[23] S. Bressler, L. Moleri, L. Arazi, E. Erdal, A. Rubin, M. Pitt, and A. Breskin. A concept for laboratory studies of radiation detectors over a broad dynamic-range: instabilities evaluation in THGEM-structures. *JINST*, 9:P03005, 2014.

[24] L.W. Nagel and D. O. Pederson. Simulation Program with Integrated Circuit Emphasis - SPICE. *Univeristy of California, Berkeley*, Memorandum No. ERL-M382, Apr. 1973.

[25] C. Adloff et al. MICROMEGAS chambers for hadronic calorimetry at a future linear collider. *JINST*, 4:P11023, 2009.

[26] S. Agostinelli et al. GEANT4: A Simulation toolkit. *Nucl. Instrum. Meth. A*, 506:250–303, 2003.

[27] C. Adloff et al. Test in a beam of large-area Micromegas chambers for sampling calorimetry. *Nucl. Instrum. Meth. A*, 763:221–231, 2014.

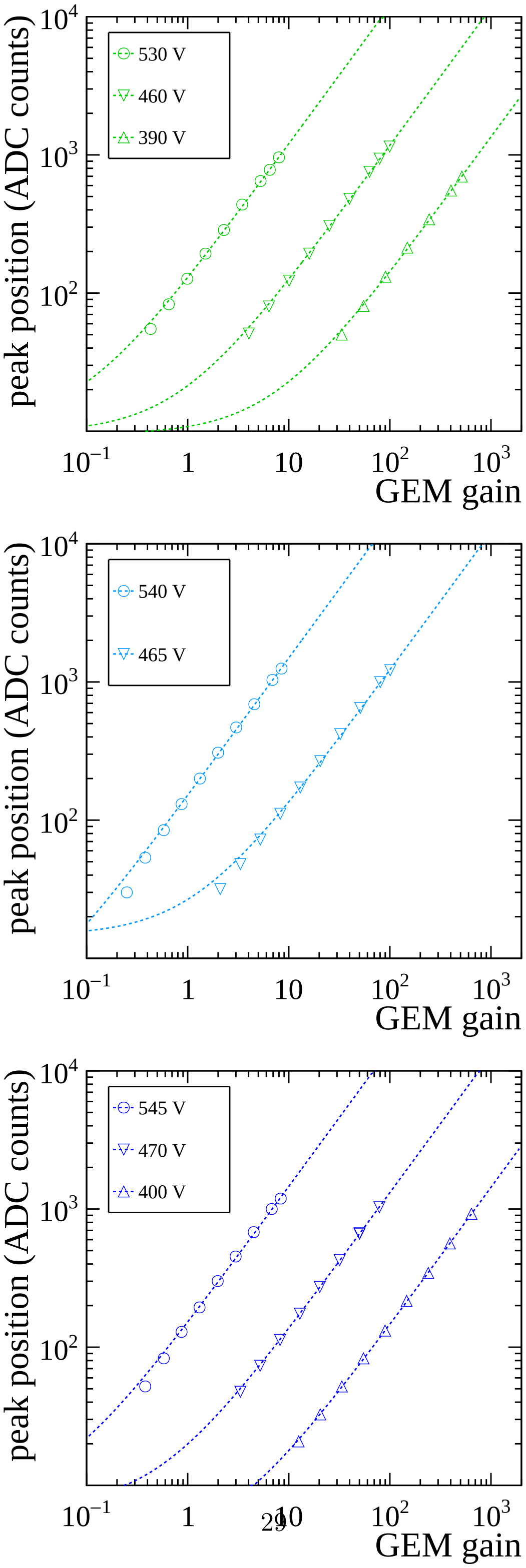

Figure 7: Response of $100\,\mathrm{k}\Omega/\square$ resistive prototypes to ^{55}Fe quanta when using a GEM foil as pre-amplification stage. From top to bottom: star, mirror and snake patterns. Dashed lines are linear functions to guide the eye. The double logarithmic scale is chosen for the sake of readability.

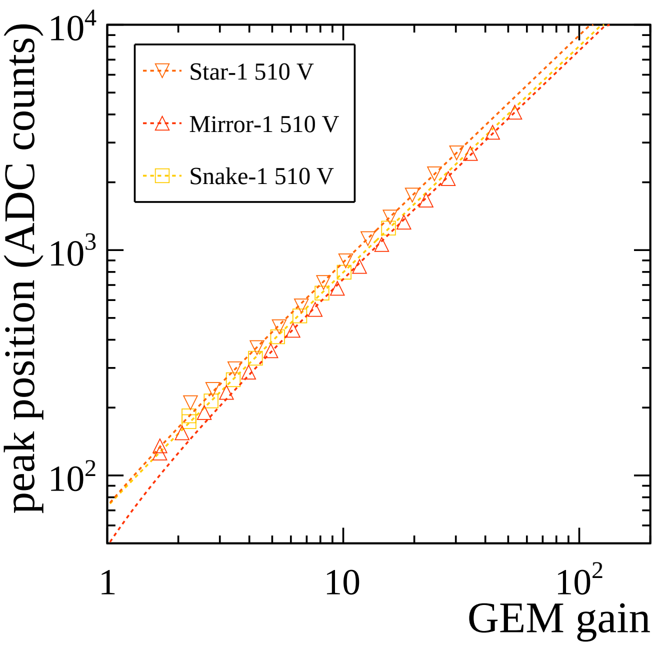

Figure 8: Response of $1\,\mathrm{k}\Omega/\square$ resistive prototypes to ^{55}Fe quanta when using a GEM foil as pre-amplification stage. Dashed lines are linear functions to guide the eye.

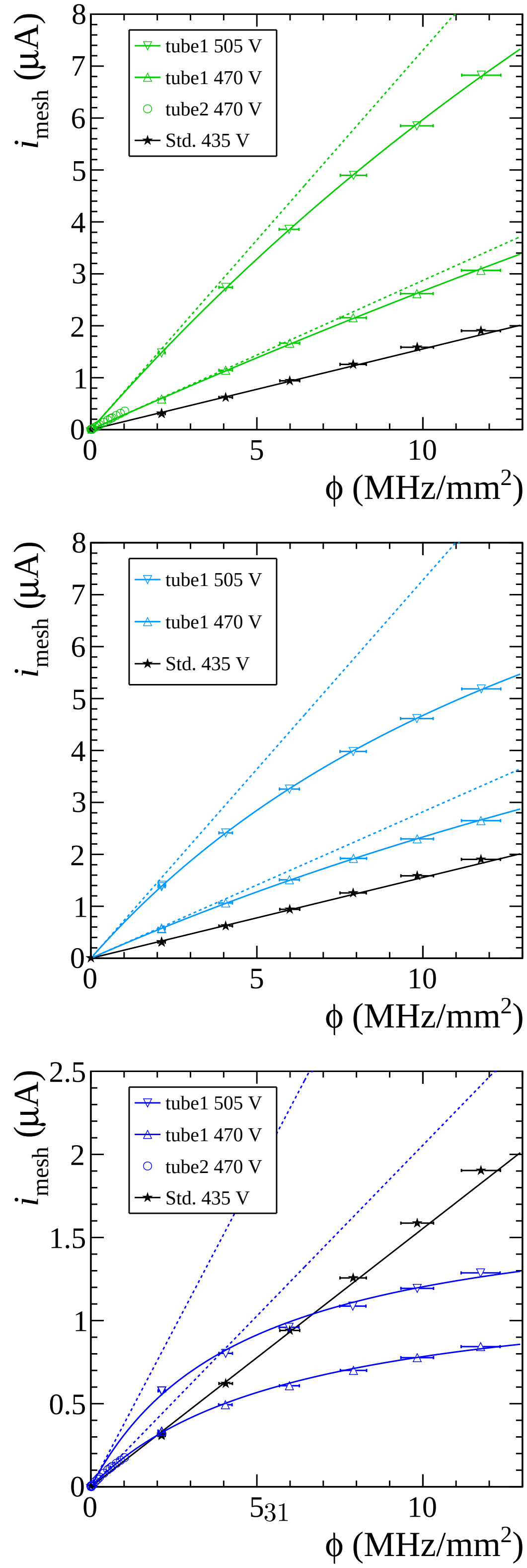

Figure 9: Rate capability of 100 kΩ/□ resistive prototypes. From top to bottom: star, mirror and snake-like resistor pattern. Plain lines are a fit of Eq. 3 to the data points and dashed lines are the expected response in the absence of charge-up. Points and lines in black color are the best measurement performed with a standard non-resistive prototype.

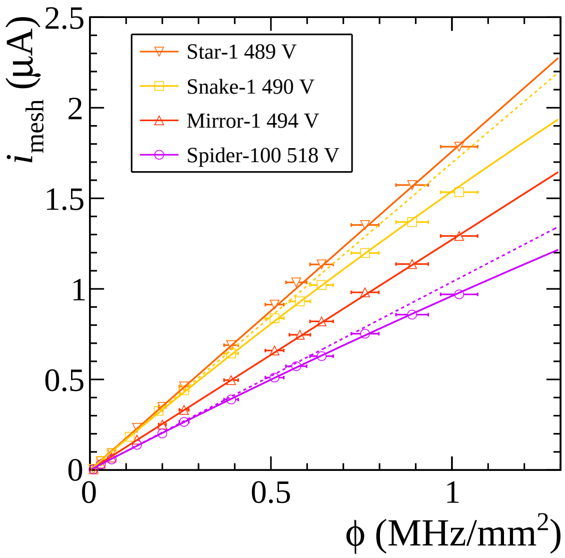

Figure 10: Rate capability of 1 kΩ/□ resistive prototypes. Plain lines are the fits of Eq. 3 to the data points and dashed lines are the expected response in the absence of charge-up.

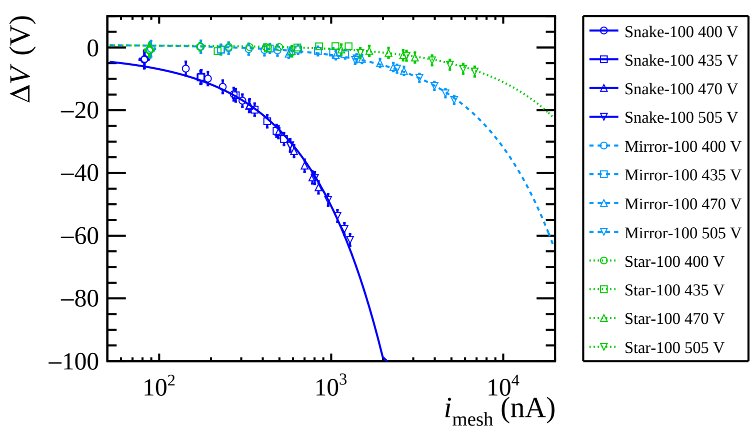

Figure 11: Rate capability of 100 kΩ/□ resistive prototypes plotted as a voltage to current dependence. Markers are data points. Lines are a fits of a linear function to the data and represent Ohm's law.

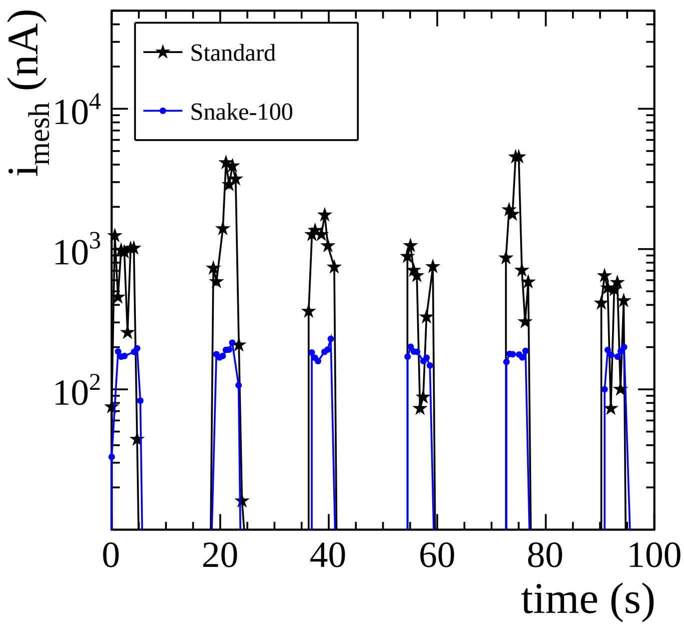

Figure 12: Mesh current under periodic pion irradiation.

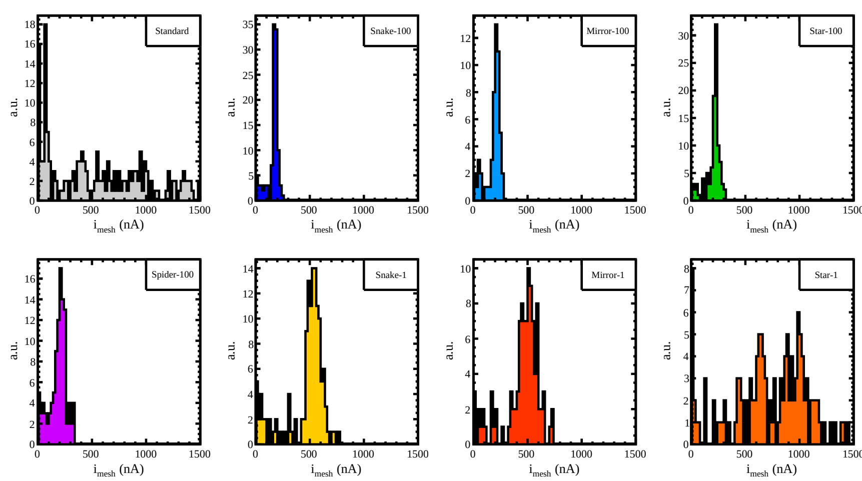

Figure 13: Mesh current at high pion rate in the H4 SPS beam line at CERN.

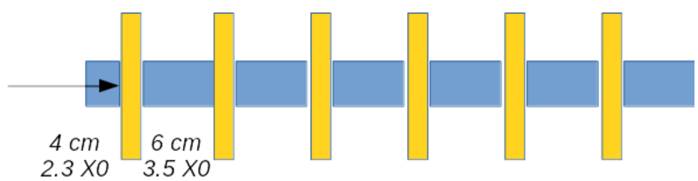

Figure 14: Sketch of the small calorimeter. Iron absorbers and Micromegas prototypes are colored in blue and yellow respectively. The arrow indicate the direction of the beam.

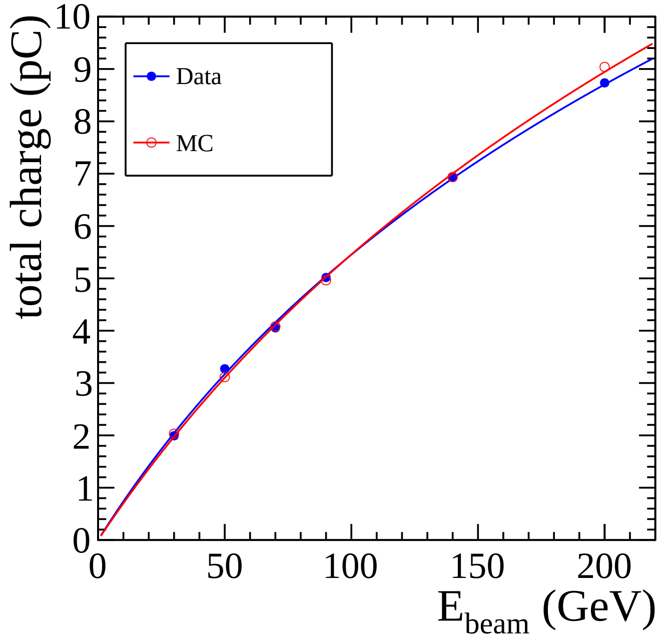

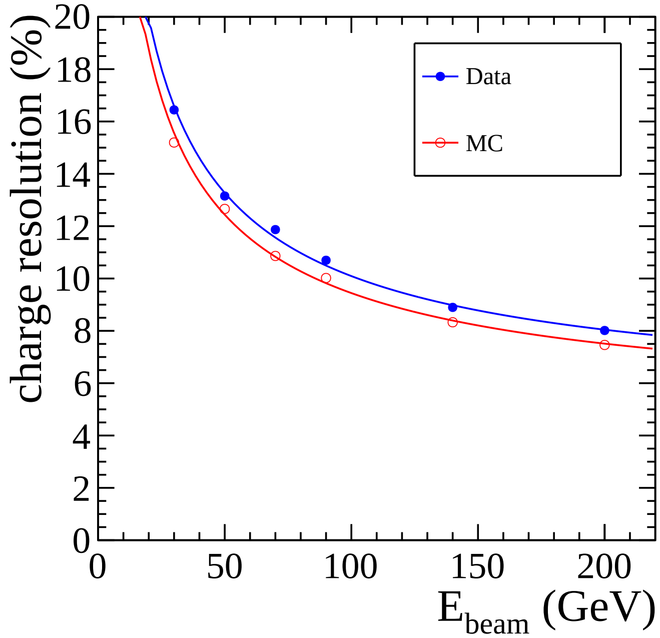

Figure 15: Electron response (top) and charge fluctuations (bottom) of a small sampling Micromegas calorimeter.

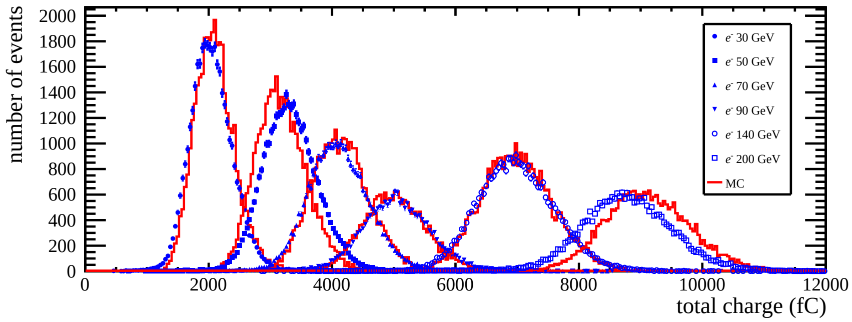

Figure 16: Total charge from electrons showering in a small sampling Micromegas calorimeter. Different markers indicate different energy of the beam. Simulation results are plotted as red histograms.

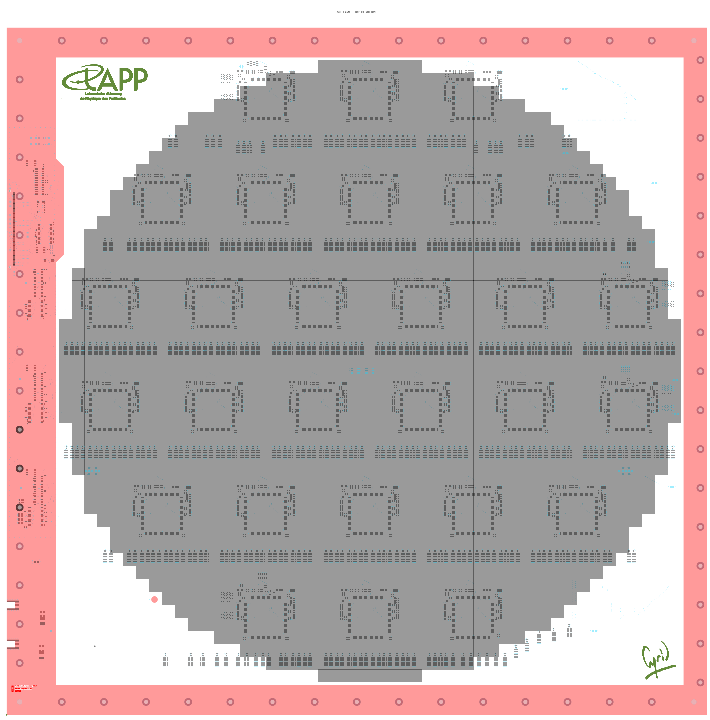

Figure 17: ASU design with 28 ASICs represented as black squares and 1792 pads forming a circular active area (drawn in in grey). The red perimeter is used for mechanical assembly, powering and connection to the readout.

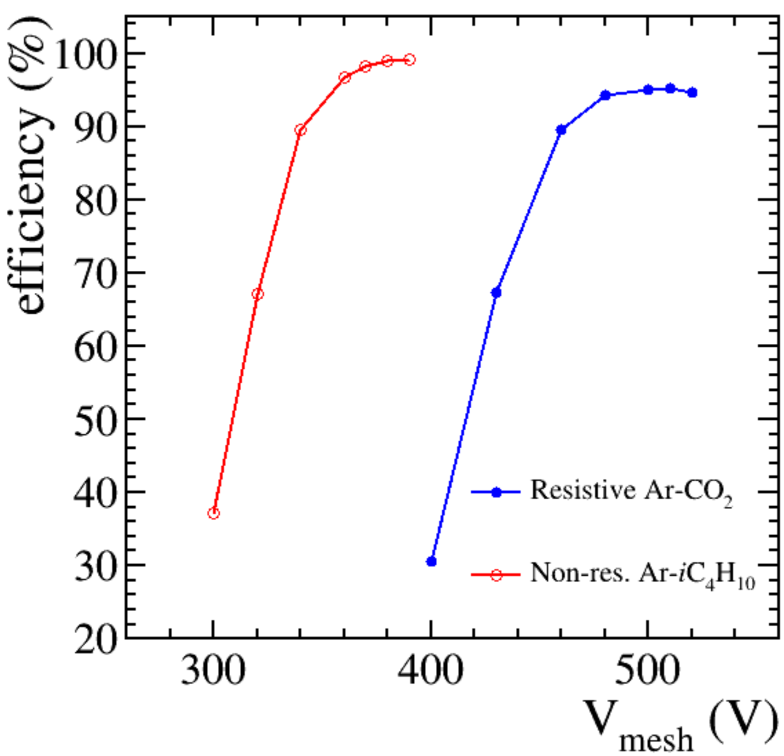

Figure 18: Muon efficiency using resistive and non-resistive ASUs and a different gas mixture).

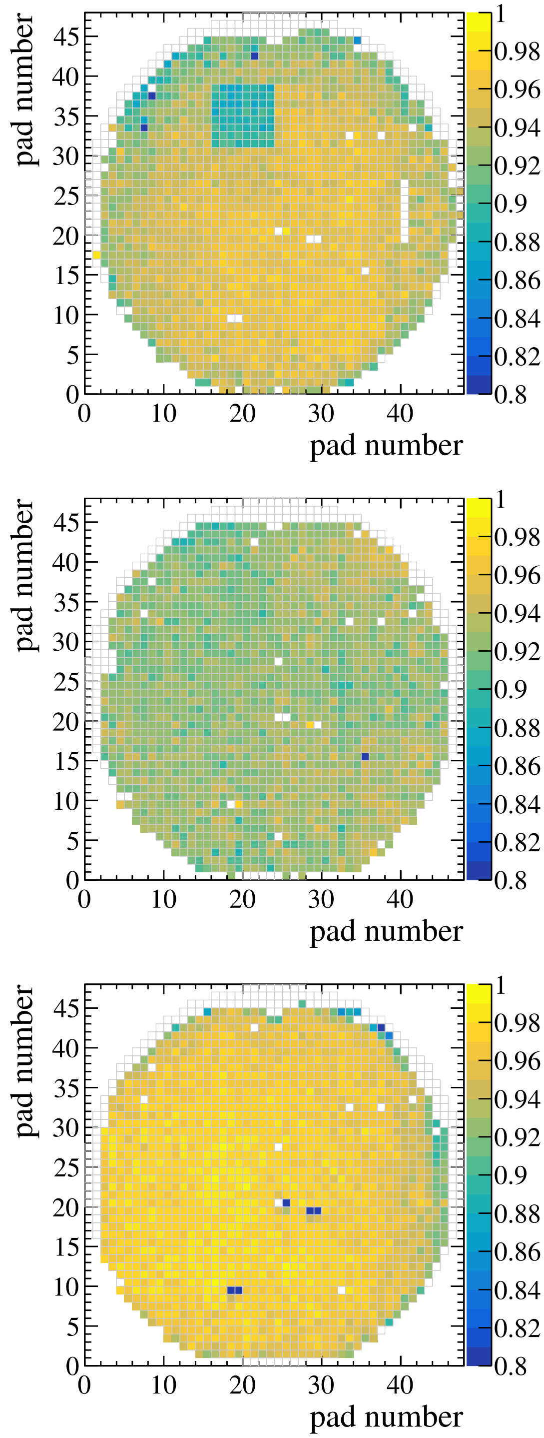

Figure 19: Efficiency maps of the three resistive ASU operated at 500 V.

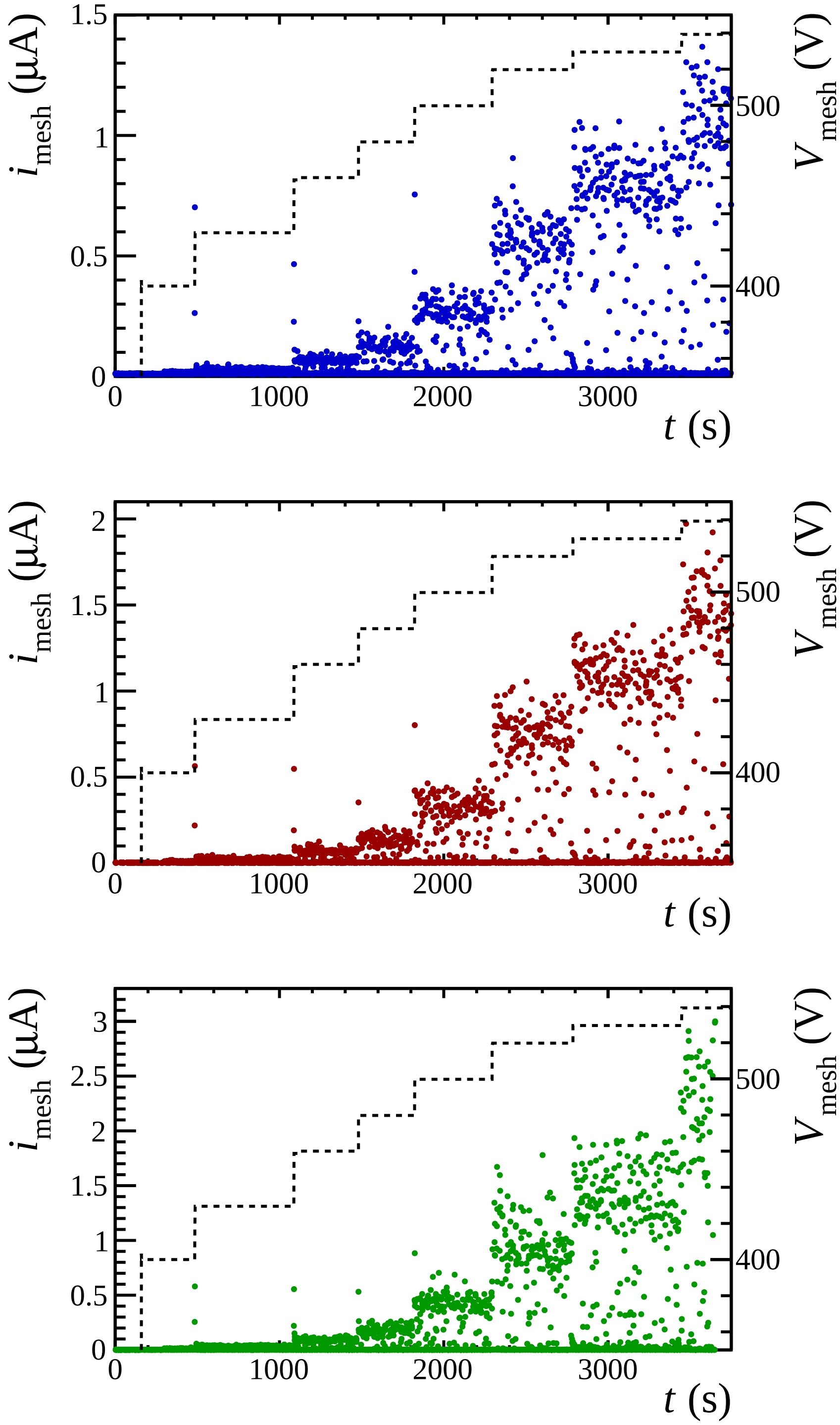

Figure 20: Mesh current during intense pion irradiation at increasing mesh voltages. The most upstream (downstream) prototype on the beam line is plotted at the top (bottom). Colored points stand for measured mesh currents and reflect the time structure of the pion spills, dashed lines indicate voltage settings.